Magnetoelastic hybrid excitations in $CeAuAl_3$

Petr Čermák[a,b,1], Astrid Schneidewind[b], Benqiong Liu[c], Michael Marek Koza[d], Christian Franz[e,f], Rudolf Schönmann[f], Oleg Sobolev[g], and Christian Pfleiderer[f,1]

[a]Faculty of Mathematics and Physics, Department of Condensed Matter Physics, Charles University, 121 16 Praha, Czech Republic; [b]Forschungszentrum Jülich GmbH, Jülich Centre for Neutron Science at Heinz Maier-Leibnitz Zentrum, 85748 Garching, Germany; [c]Key Laboratory of Neutron Physics, Institute of Nuclear Physics and Chemistry, China Academy of Engineering Physics, Mianyang 621900, People's Republic of China; [d]Institut Laue Langevin, 38042 Grenoble, France; [e]Heinz Maier-Leibnitz Zentrum, Technische Universität München, 85748 Garching, Germany; [f]Physik-Department, Technische Universität München, 85748 Garching, Germany; and [g]Institute for Physical Chemistry, Georg-August-University of Göttingen, D-37077 Göttingen, Germany

Edited by Zachary Fisk, University of California, Irvine, CA, and approved February 15, 2019 (received for review November 17, 2018)

Nearly a century of research has established the Born–Oppenheimer approximation as a cornerstone of condensed-matter systems, stating that the motion of the atomic nuclei and electrons may be treated separately. Interactions beyond the Born–Oppenheimer approximation are at the heart of magneto-elastic functionalities and instabilities. We report comprehensive neutron spectroscopy and ab initio phonon calculations of the coupling between phonons, CEF-split localized 4*f* electron states, and conduction electrons in the paramagnetic regime of $CeAuAl_3$, an archetypal Kondo lattice compound. We identify two distinct magneto-elastic hybrid excitations that form even though all coupling constants are small. First, we find a CEF–phonon bound state reminiscent of the vibronic bound state (VBS) observed in other materials. However, in contrast to an abundance of optical phonons, so far believed to be essential for a VBS, the VBS in $CeAuAl_3$ arises from a comparatively low density of states of acoustic phonons. Second, we find a pronounced anticrossing of the CEF excitations with acoustic phonons at zero magnetic field not observed before. Remarkably, both magneto-elastic excitations are well developed despite considerable damping of the CEFs that arises dominantly by the conduction electrons. Taking together the weak coupling with the simultaneous existence of a distinct VBS and anticrossing in the same material in the presence of damping suggests strongly that similarly well-developed magneto-elastic hybrid excitations must be abundant in a wide range of materials. In turn, our study of the excitation spectra of $CeAuAl_3$ identifies a tractable point of reference in the search for magneto-elastic functionalities and instabilities.

magneto-elastic coupling | f-electron materials | neutron spectroscopy | Kondo lattice materials | crystal electric field

The interactions between elementary excitations such as phonons, plasmons, magnons, or particle–hole pairs drive emergent functionalities and electronic instabilities such as multiferroic behavior (1), anomalous thermoelectric properties (2), polar order (3), or superconductivity (4). However, the interplay of the underlying energy scales, namely phonons, crystal electric field (CEF) excitations, particle–hole pairs, spin–orbit coupling, and magnetic interactions, typically tends to be of a similar strength characteristic to that of a veritable chicken-and-egg type of problem. In turn, a key question concerns the possible existence of coupling phenomena in systems featuring weak interactions in the absence of electronic instabilities, such as magnetic or multipolar order, as well as structural instabilities. In this limit the electronic degrees of freedom reduce to the CEFs as well as the conduction electrons (for the case of metals), and the Born–Oppenheimer approximation (5) may be readily expected to be valid.

Whereas the conventional properties of the CEF excitations in such a pristine environment are well documented, longstanding questions concern the formation of additional excitations beyond the single-ion level, as well as finite lifetimes and anomalous temperature dependences. Two primary mechanisms have been considered. First, phonons may create CEF transitions between neighboring ions (6), representing an important example of so-called magneto-elastic (ME) coupling in the absence of magnetic order (7–10). Second, in metallic systems a coupling exists with particle–hole excitations (11). While various facets of the CEFs have been studied extensively, experimental information on the coupling strengths as well as the full range of properties of the CEFs is remarkably limited due to a lack of high-resolution single-crystal data (12–17).

Paramagnetic rare-earth intermetallics with weak ME coupling are particularly suited to resolve these questions, as both spin and orbital angular contributions generate the ME coupling, and the well-defined multiplet structure of the f shells makes the ME coupling tractable (18). For instance, formation of a vibronic bound state (VBS) between phonons and CEF excitations has been reported in $CeAl_2$ (19–22). Similar VBSs have also been proposed to exist in $PrNi_2$ (23), $Ce_3Pt_{23}Si_{11}$ (24), $CePd_2Al_2$ (13, 25), and $CeCuAl_3$ (14) as well as rare-earth doped cuprates (26) and geometrically frustrated oxides (8, 15, 27). However, as the phonon density of states must be large, it is generally believed that the VBS may be formed only with weakly dispersive optical phonons. This raises the question of the origin of unexplained excitations at momentum transfers away from the Γ point (28), the nature of inconsistencies of presently known VBSs with light scattering (29, 30), and whether ME-hybrid modes may be

Significance

A cornerstone of condensed-matter physics is the Born–Oppenheimer approximation, which assumes that the motion of the atomic nuclei and electrons in solids may be treated separately. We report the observation of two distinct magneto-elastic hybrid excitations of the phonons and crystal electric fields (CEFs) in the paramagnetic state of the Kondo lattice compound $CeAuAl_3$: (*i*) a vibronic bound state and (*ii*) a pronounced anticrossing. The formation of both excitations due to acoustic phonons in the presence of small coupling constants, as well as considerable damping of the CEF excitations by the conduction electrons, suggests that similar hybrid excitations must generically exist in a wide range of materials. This identifies $CeAuAl_3$ as a showcase for the development of a predictive understanding of magneto-elastic instabilities.

Author contributions: P.Č., A.S., and C.P. designed research; P.Č., A.S., B.L., M.M.K., C.F., R.S., and O.S. performed research; P.Č. and B.L. analyzed data; and P.Č. and C.P. wrote the paper.

The authors declare no conflict of interest.

This article is a PNAS Direct Submission.

Data deposition: The data reported in this paper are available from figshare (https://figshare.com/articles/Magnetoelastic_hybrid_excitations_in_CeAuAl3/7803092/2).

[1]To whom correspondence may be addressed. Email: christian.pfleiderer@tum.de or cermak@mag.mff.cuni.cz.

This article contains supporting information online at www.pnas.org/lookup/suppl/doi:10.1073/pnas.1819664116/-/DCSupplemental.

generic in paramagnets and driven by the full spectrum of optical and acoustic phonons (18).

On a related note, formation of an anticrossing, also referred to as level repulsion, representing a different ME-hybrid mode has been suggested at the intersection of acoustic phonons and CEF excitations in Pr and $\mathrm{PrAl_2}$ under an applied magnetic field and the magnetically ordered state of $\mathrm{TmVO_4}$, where they are mediated by dipolar interactions (31–36). In comparison, a generic anticrossing in zero magnetic field between phonons and CEFs that is mediated by quadrupolar interactions in a paramagnetic state has been predicted only theoretically. Putative evidence for the latter may have been observed in the insulators $\mathrm{PrAlO_3}$ (37) and $\mathrm{TbVO_4}$ (38); in the rare-earth (RE) compound $\mathrm{PrNi_5}$ the evidence is indirect (39, 40).

The formation of well-defined ME-hybrid modes is constrained by the lifetime and temperature dependence of CEF excitations, which deviates in many materials from the expected thermal population of single-ion states (41–46). In a seminal theoretical study Becker, Fulde, and Keller (BFK) (11) successfully attributed the anomalous temperature dependences of the CEF occupation to the interaction with particle–hole pairs in metallic systems. Interestingly, these interactions may mediate superconductive pairing as proposed in $\mathrm{UPd_2Al_3}$ (44, 45, 47, 48) and $\mathrm{PrOs_4Sb_{12}}$ (49).

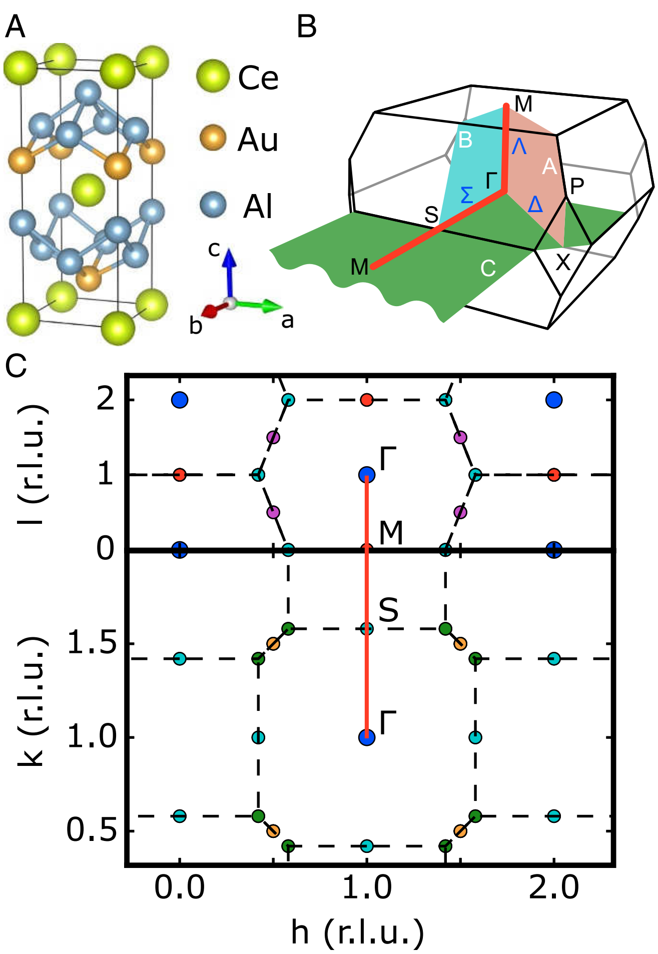

Fig. 1. Depiction of key characteristics of $\mathrm{CeAuAl_3}$ in real and reciprocal space. (*A*) Crystallographic unit cell of $\mathrm{CeAuAl_3}$. The tetragonal $\mathrm{BaNiSn_3}$ structure (space group *I4mm*, no. 107) lacks inversion symmetry (50–52). (*B*) Brillouin zone of a body-centered tetragonal lattice (where $c > a$). High-symmetry positions are marked according to the Bilbao notation (53), where points, lines, and planes are denoted by black, blue, and white letters, respectively. (*C*) (*h*, *k*, 0) and (*h*, 0, *l*) planes in reciprocal space. Locations at which data were recorded are marked by a red line.

In this paper we report a comprehensive single-crystal inelastic neutron scattering study of the low-lying excitations and ab initio phonon calculations in the paramagnetic state of $\mathrm{CeAuAl_3}$ (Fig. 1*A*), a member of the $\mathrm{CeTAl_3}$ series (T = Ce, Au, Pd, Pt) and thus the wider family of $\mathrm{BaAl_4}$-type materials (52). Early measurements of the bulk and transport properties of polycrystalline samples established $\mathrm{CeAuAl_3}$ as a Kondo lattice compound stabilizing incommensurate antiferromagnetic order below $T_\mathrm{N} = 1.32$ K (50, 54). The enhancement of the linear temperature dependence of the specific heat and quadratic temperature dependence of the resistivity ($\gamma = 227$ mJ·mol^{-1}·K^{-2} and $A = 5\ \mu\Omega\mathrm{cm}\cdot\mathrm{K}^{-2}$, respectively) are characteristic of a heavy Fermi liquid state. The CEF lifts the degeneracy of the Ce^{3+} $J = 5/2$ manifold directly as seen in the magnetic susceptibility and specific heat. However, the first and second doublets at $T_\mathrm{I} = 57\,\mathrm{K}$ and $T_\mathrm{II} = 265\,\mathrm{K}$ are split from the ground state such that they have no bearing on the bulk properties and the enhancement of the Fermi liquid ground state. An unusual feature is a reduced anisotropic thermal conductivity attributed to ME phonon scattering of the Ce ions (55).

The observation of a VBS in $\mathrm{CePd_2Al_2}$ (13), a related tetragonal compound, appears to be intimately related to a structural phase transition and suggests a strong interplay of the CEF excitations and phonons in this class of systems. Indeed, time-of-flight (TOF) neutron spectroscopy revealed also a VBS in polycrystalline $\mathrm{CeCuAl_3}$ (14) confirmed recently in single-crystal spectroscopy (56) and in slightly off-stoichiometric samples (57). Here, too, electronic excitations are assumed to hybridize with optical phonons, which results in four doublets: $|\Gamma_6, 0\rangle$, $|\Gamma_6, 1\rangle$, and $|\Gamma_7^{1,2}, 0\rangle$. This suggests that the symmetry of the lattice fluctuations imparts a different character on the VBS in tetragonal compared with cubic systems. However, systematic time-of-flight neutron spectroscopy in polycrystalline $\mathrm{CeRhGe_3}$ (58) and $\mathrm{CeAuAl_3}$ (54) failed to detect a VBS. Moreover, the search for ME phonon softening by inelastic X-ray scattering in $\mathrm{CeCuAl_3}$ and $\mathrm{CeAuAl_3}$ has been inconclusive (59).

Results

Shown in Fig. 1*B* is the first Brillouin zone (BZ) of the body-centered tetragonal unit cell of $\mathrm{CeAuAl_3}$. The relevant (h, k, 0) and (h, 0, l) planes and the trajectory of our measurements in reciprocal space are indicated by a red line in Fig. 1 *B* and *C*. Starting at the Γ point, this trajectory proceeded along the c axis toward the zone boundary at the M point, followed by the line connecting the M and the S points in the ab plane, before returning to the Γ point. Since these directions of momentum transfer do not coincide with the main crystallographic orientations of the primitive unit cell, neutrons couple to all polarizations of the phonon modes. This proves to be helpful in the interpretation of our data presented below.

An overview of the excitation spectra of $\mathrm{CeAuAl_3}$ as a function of reduced scattering wave vector $\mathbf{q}$ is presented in Fig. 2*A*. All data were recorded at a temperature of 5 K or higher, in the paramagnetic state well above T_N. For any reduced scattering vector q, the spectra feature two flat excitations, marked by red and green shading. The flat excitations are crossed by strongly dispersive phonon modes branching out of the Γ points. The interplay of the acoustic phonons with the flat excitations features the two main experimental findings of our study, notably (*i*) formation of a VBS as marked by green shading and (*ii*) well-resolved anticrossing of acoustic phonons with the crystal field along the Γ to M direction shown in Fig. 2*C*. Both excitations are rather distinct despite considerable broadening of the crystal-field levels with increasing temperature as shown in Fig. 3 and discussed below.

The crystal-field excitation at $E_\mathrm{CF} = 4.9\,\mathrm{meV}$ (Fig. 2*A*, red shading) may be attributed to the transition from the $|\Gamma_6\rangle$ ground

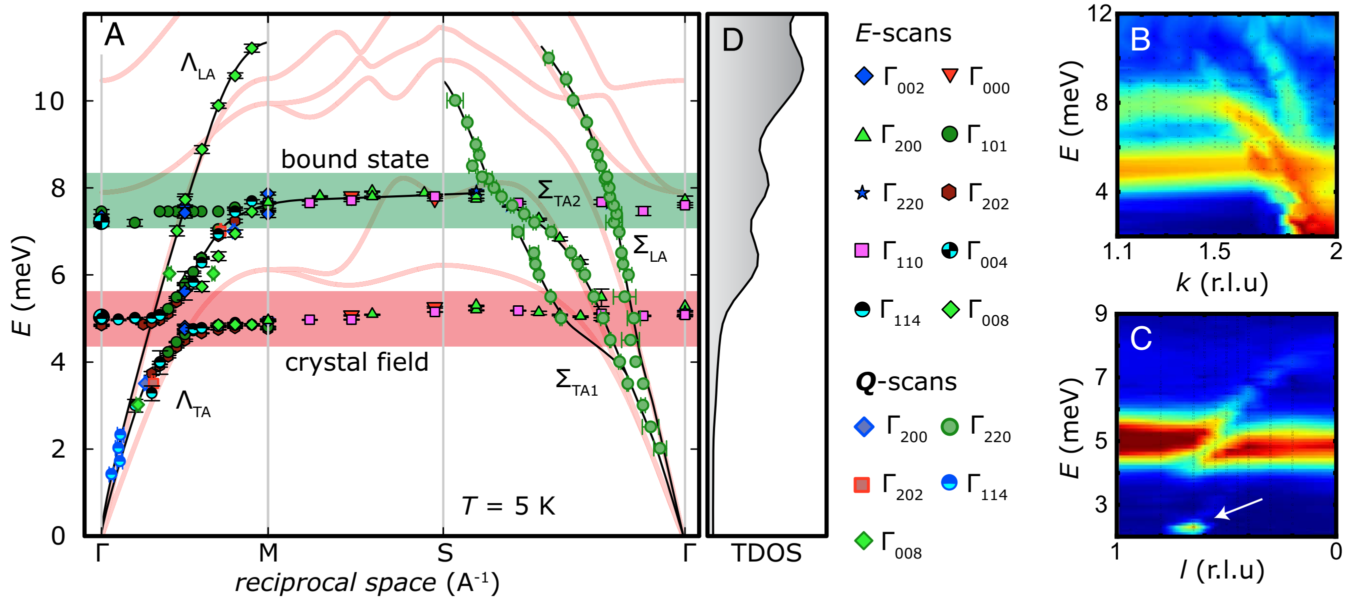

Fig. 2. Key characteristics of the neutron-scattering excitation spectra of single-crystal $CeAuAl_3$ observed in reciprocal space along Γ to *M* to *S* to Γ at *T* = 5 K. (*A*) Energy vs. reciprocal space map of $CeAuAl_3$. Data points represent the peak positions of Gaussian fits (energy scans are denoted by a black border; momentum scans are denoted by a colored border). Blue, red, and green shading denotes the Brillouin zone in which data were recorded (see Fig. 4). The plots display the location of maxima only, but not the strength of the intensities. Red lines in background represent the results of ab initio phonon calculations, where the f electrons were treated as valence electrons (60). (*B*) Intensity map inferred from excitation spectra recorded between *M* and Γ along (2, *k*, 0). Above the crystal field excitations around 5 meV a magneto-elastic hybrid excitation emerges around 8 meV. (*C*) Intensity map inferred from excitation spectra recorded between Γ and *M* along (1, 0, *l*). A clear anticrossing is observed. The feature marked by a white arrow represents spurious Bragg scattering. (*D*) Calculated phonon density of states (compare red lines in *A*). Maxima are observed at 6 meV, 8 meV, and 11 meV, consistent with the bound state at $E_{VBS} = 7.9$ meV. The black line and color shading serve to guide the eye.

state to the first excited doublet $|\Gamma_7^1\rangle$ (compare Fig. 2*B*). The energy of this transition is in excellent agreement with previous time-of-flight neutron spectroscopy and bulk data in a polycrystalline sample, which, however, did not allow a search for a momentum dependence (50, 54). The weak nondispersive excitation at $E_{VBS} = 7.9\,\text{meV}$ (Fig. 2*A*, green shading) is an unexpected characteristic. It was not observed in previous time-of-flight neutron spectroscopy studies (54), probably due to the loss in spectral weight in the polycrystalline average.

The strongly dispersive excitations at the Γ points may be clearly attributed to acoustic phonons as they emanate from nuclear Bragg peaks. Taking into account the tetragonal crystal symmetry, a longitudinal and a transverse acoustic branch are observed along the Γ to *M* direction, labeled as Λ_{LA} and Λ_{TA}, respectively. As illustrated in Fig. 2*C*, these phonons display compelling evidence of an anticrossing with the crystal-field excitation at E_{CF} in the three independent Brillouin zones studied, namely (101), (202), and (114) (*SI Appendix*). In contrast, for the Γ to *S* direction (labeled Σ) the two nondegenerate transverse acoustic phonons and a longitudinal acoustic phonon, denoted Σ_{TA1}, Σ_{TA2}, and Σ_{LA}, respectively, cross the nondispersive excitations at E_{CF} and E_{VBS} without apparent interaction (Fig. 2*B*). We could not identify any evidence for phonons in the vicinity of the zone boundary between the *M* and *S* points, either because the intensity was too low or because they coincided with the VBS. The intensity marked by the white arrow in Fig. 2*C* is a so-called Currat–Axe spurion, which is a well-known artifact in triple-axis spectroscopy.

The momentum dependence of the intensity of the dispersionless excitations at E_{CF} and E_{VBS} follows from the form factor of the Ce^{3+} ion (*SI Appendix*, Fig. S6). This provides strong evidence that these excitations are essentially magnetic. By contrast, the strongly dispersive excitations at the Γ points are essentially due to nuclear scattering. Moreover, as a function of increasing temperature the intensity of both dispersionless excitations decreases strongly as shown in Fig. 3 *A–C*. This is qualitatively consistent with the thermal population of the first excited crystal-field level and provides further evidence for a magnetic character of these excitations. However, closer inspection reveals that the intensity decreases much faster than would be

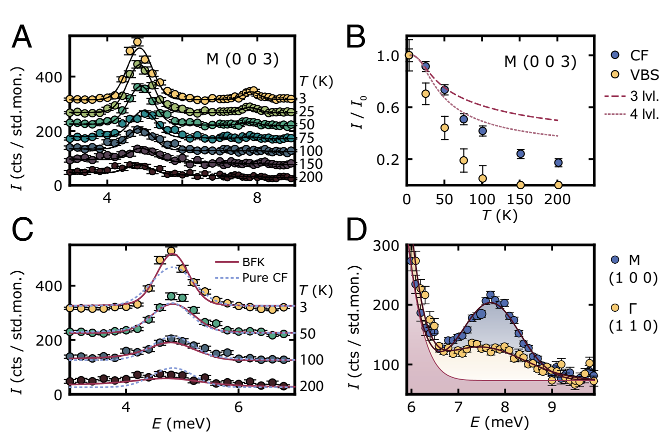

Fig. 3. Temperature dependence of the CEF and VBS at $E_{CF} = 4.9$ meV and $E_{VBS} = 7.9$ meV, respectively. (*A*) Energy scans at the *M* point at (003) for various temperatures. Scans are shifted vertically by 60 counts for clarity. Solid lines represent two independent Gaussians. (*B*) Integrated intensity of the CEF and vibronic bound state normalized to 3 K. Red dashed lines show the calculated temperature dependence at the *M* point for a three- and a four-level system. (*C*) Selected scans shown in *A* as fitted with a pure crystal-field model with fixed intensities in a three-level model (dotted lines) and a model based on the BFK model (11) (solid lines). (*D*) Energy scans through the VBS at the Γ and the *M* point. Dark solid lines represent a Gaussian fit to the data. Red shading denotes the background and the pure crystal-field excitation.

expected of a simple three-level system. This may be attributed to dominant hybridization with the conduction electrons as discussed below.

As illustrated by the energy scans at the Γ and M points shown in Fig. 3*D*, the dispersionless excitation at $E_{\mathrm{VBS}} = 7.9\,\mathrm{meV}$ varies strongly in intensity throughout the Brillouin zone. The intensity is large at the zone boundary and becomes very weak and difficult to discern at the zone center as observed in all Brillouin zones investigated and listed in Fig. 2*A*. In stark contrast, no such variation was observed for the dispersionless excitation at $E_{\mathrm{CF}} = 4.9\,\mathrm{meV}$, except near the Γ point in the (101) Brillouin zone (*SI Appendix*, Fig. S7). Thus, the formation of the dispersionless excitation at $E_{\mathrm{VBS}} = 7.9\,\mathrm{meV}$, as well as the enhancement of the excitation at $E_{\mathrm{CF}} = 4.9\,\mathrm{meV}$ at the Γ point, is driven by a coupling to phonons.

Discussion

For the discussion of our experimental results we assume that the magneto-elastic properties in the paramagnetic state of $\mathrm{CeAuAl_3}$ are dominated by the interactions of the $4f$ electrons with the electrostatic crystal field. A Hamiltonian describing this situation is given by $H = H_{\mathrm{L}} + H_{\mathrm{CF}} + H_{\mathrm{ME}}$, where H_{L} accounts for the kinetic and potential energy of the Bravais lattice, H_{CF} denotes the conventional crystal-field Hamiltonian, and H_{ME} represents the single-ion magneto-elastic coupling of the spin to lattice strains. It is important to note that the phonons and CEF excitations must share the same symmetry to couple directly.

Treating the contribution of the Bravais lattice, H_{L}, in a harmonic approximation we calculated the structural properties and spectrum of phonon excitations (60) using the Vienna ab initio simulation package (VASP) in the frozen-core projector augmented wave (PAW) method. The calculated lattice constants $a = 4.335\,\mathrm{Å}$ and $c = 10.844\,\mathrm{Å}$ were found to be in excellent agreement with experiment (52). Further, the spectrum of phonon excitations was calculated using a finite-difference method. The results are shown as shaded red lines in Fig. 2*A* for energies up to $12\,\mathrm{meV}$ and also as total density of phonon states in Fig. 2*D*. For the five atoms in the primitive unit cell of $\mathrm{CeAuAl_3}$ the full phonon dispersion consists of 15 branches, which comprise 3 acoustic and 12 optical modes. Using group theoretical techniques, an analysis of the irreducible representations for the high-symmetry points establishes that the two acoustic branches along Γ to Z are degenerate. This justifies the assignment of the phonon branches in the vicinity of the Γ points. At low energies the phonon branches are in excellent agreement with calculation. However, in the range 4–9 meV we observe systematic deviations highlighting the presence of ME coupling.

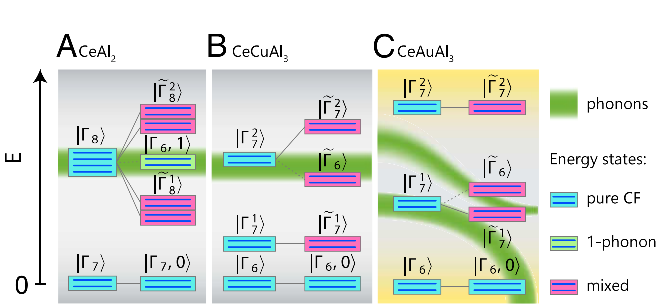

Fig. 4. Comparison of CEF–phonon excitations and emergence of ME-hybrid states in selected f-electron materials. Energy scales are normalized to the highest transition. (*A*) VBS in $\mathrm{CeAl_2}$. Under the action of the three ME operators $\mathcal{O}_{1,2,3}$ the unperturbed $|\Gamma_8\rangle$ splits into five doublets and a VBS forms where the CEF coincides with an optical phonon (19, 21, 65). (*B*) ME-hybrid excitation in $\mathrm{CeCuAl_3}$. Under the ME operator $\mathcal{O}_2^2$ the unperturbed doublet $|\Gamma_7, 1\rangle$ splits into two doublets with an additional VBS (14). (*C*) ME effects in $\mathrm{CeAuAl_3}$, notably a VBS, anticrossing, and CEF damping due to conduction electrons. The phonon density of states (green shading) illustrates the dispersive phonon modes.

Table 1. Coupling constants compared with literature values

Compound	g_{VBS}, μeV	g_{AC}, μeV	g_{BFK}, dimensional	Source
$\mathrm{CeAuAl_3}$	≈ 400	12.1(2)	0.022(0)	This study
$\mathrm{CeAl_2}$	540		0.06	(22)
$\mathrm{CeCuAl_3}$	800			(14)
$\mathrm{PrNi_5}$		<4*		(39)

*This value was obtained by fitting the data reported in ref. 39; see also *SI Appendix*, Fig. S6.

For the tetragonal symmetry of $\mathrm{CeAuAl_3}$, point group C_{4v} ($4mm$), contributions of the $\mathrm{Ce^{3+}}$ ions in the presence of a CEF may be expressed as $H_{\mathrm{CF}}^0 = B_2^0 O_2^0 + B_4^0 O_4^0 + B_4^4 O_4^4$, where B_n^m and O_n^m are the crystal electric-field parameters and Steven's operators, respectively (61, 62). Due to the symmetry constraints all parameters should be real numbers (63). In the paramagnetic phase the sixfold degenerate $4f^1$ states of $\mathrm{Ce^{3+}}$ ($J = \frac{5}{2}$) split into three doublets. For our neutron data we find $B_2^0 = 1.203\,\mathrm{meV}$, $B_4^0 = -0.001\,\mathrm{meV}$, and $B_4^4 = \pm 0.244\,\mathrm{meV}$. This corresponds to a $|\Gamma_6\rangle$ doublet ground state and two excited states, $|\Gamma_7^1\rangle$ and $|\Gamma_7^2\rangle$, at energies of 4.95 meV and 24.3 meV, respectively. The associated eigenvectors are $|\Gamma_6\rangle = |\pm\frac{1}{2}\rangle$, $|\Gamma_7^1\rangle = -\alpha|\mp\frac{3}{2}\rangle + \beta|\pm\frac{5}{2}\rangle$, and $|\Gamma_7^2\rangle = \alpha|\mp\frac{5}{2}\rangle + \beta|\pm\frac{3}{2}\rangle$, with $\alpha = 0.931$, $\beta = 0.364$. These results are in excellent agreement with neutron time-of-flight spectroscopy of a powder sample of $\mathrm{CeAuAl_3}$ (54) as well as with the bulk properties (50). Further details of the CEF analysis may be found in *SI Appendix*.

The calculations of the phonon spectrum and CEF levels presented so far clearly identify the dispersionless excitation at $E_{\mathrm{VBS}} = 7.9\,\mathrm{meV}$ (green shading in Fig. 2*A*) as an additional state. It is tempting to interpret this excitation in terms of a VBS as observed in $\mathrm{CeAl_2}$ and $\mathrm{CeCuAl_3}$. A comparison of the associated energy-level scheme of $\mathrm{CeAl_2}$ and $\mathrm{CeCuAl_3}$ with $\mathrm{CeAuAl_3}$ is shown in Fig. 4. For the cubic crystal structure of $\mathrm{CeAl_2}$, the $|\Gamma_7\rangle$ doublet and $|\Gamma_8\rangle$ quartet of cerium in the CEF form a set of new eigenstates. By virtue of hybridization with optical phonons, this yields one electronic $|\Gamma_7, 0\rangle$, one phononic $|\Gamma_6, 1\rangle$ doublet, and two mixed $|\widetilde{\Gamma}_8^{1,2}\rangle$ quartets, which are linear combinations of purely electronic and single-phonon states, depicted in Fig. 4*A*. Similarly, the formation of the VBS in the tetragonal crystal structure of $\mathrm{CeCuAl_3}$, illustrated in Fig. 4*B*, involves a hybridization of the $|\Gamma_7^2\rangle$ doublet with a high density of optical phonons to form a phononic $|\Gamma_6, 1\rangle$ doublet and three mixed doublets, denoted $|\widetilde{\Gamma}_6\rangle$ and $|\widetilde{\Gamma}_7^{1,2}\rangle$. Thus, in both cases the formation of a Thalmeier–Fulde VBS presumes strong ME interactions between weakly dispersive optical phonons and a nearby CEF level.

In contrast, in $\mathrm{CeAuAl_3}$ at the energy of the putative VBS the phonon calculations do not yield the required high density of states. A low phonon density of states at $E = 8\,\mathrm{meV}$, as well as $E \approx 6\,\mathrm{meV}$ and $E = 11 - 13$ meV, is also supported by our calculations [see Fig. 2*D* and neutron time-of-flight spectroscopy on polycrystalline samples of $\mathrm{LaAuAl_3}$ (54)]. This implies that one important prerequisite for the formation of a VBS is apparently absent.

In turn, our measurements imply that a weak coupling of the $|\Gamma_6\rangle$ to $|\Gamma_7^1\rangle$ excitation with acoustic phonons is sufficient for the formation of a VBS at $E_{\mathrm{VBS}} = 7.9\,\mathrm{meV}$ as illustrated in Fig. 4*C*. This implies that CEF excitations may form bound states with phonons that (*i*) do not cover large portions of the Brillouin zone, (*ii*) are dispersive, and (*iii*) are of much reduced intensity. Further, with increasing ME coupling the enhancement of the $|\widetilde{\Gamma}_7^1\rangle$

level may be expected to decrease. In contrast, the newly created $|\Gamma_6, 1\rangle$ level increases.

Using similar methods as reported in ref. 14, the coupling constant is roughly determined as $g_{\mathrm{VBS}} = 0.4\,\mathrm{meV}$ (for details see *SI Appendix*). The reduced intensity of the excitation at $E_{\mathrm{VBS}} = 7.9\,\mathrm{meV}$ compared with the excitation at $E_{\mathrm{CF}} = 4.9\,\mathrm{meV}$ implies that the low phonon density of states is just sufficient to reach the threshold for the bound state to become detectable. In fact, it is interesting to speculate whether the weak maximum of the calculated density of states at $E = 11$ meV is just below such a threshold, characteristic of an incipient VBS.

The ME interactions may also be expected to affect the spectrum of phonon and CEF excitations where they coincide (ref. (60) and *SI Appendix*). Following considerations first reported for $\mathrm{PrNi_5}$ (39) the Hamiltonian of the ME coupling, H^I_{ME}, describes the direct coupling between the deformations of the lattice and the $4f$ shell. In a group theoretical analysis (64) the energy of the coupled phonon–CEF excitation, which is mediated by quadrupolar interactions, is given by

$$\omega^2_{q\pm} = \frac{E^2 + \omega_0^2}{2} \pm \sqrt{\left(\frac{E^2 - \omega_0^2}{2}\right)^2 + 16\alpha^2 E \omega_0^2 g_{\mathrm{AC}}}, \qquad [1]$$

where $\omega_{q\pm}$ represents the energies of the two anticrossing excitations; ω_0 is the phonon energy which depends on $\boldsymbol{k}$, E is the nondispersive energy of the CEF level, and g_{AC} is an effective coupling constant related to the renormalization of the elastic constant (*SI Appendix*). A fit of our data yields g_{AC} = 12.1(2) μeV.

The ME coupling is also reflected in the temperature dependence of the scattering intensity, shown in terms of energy scans at the M point in Fig. 3*A*. It is instructive to consider the reduced scattering intensity, I/I_0, normalized to its value at low temperatures as shown in Fig. 2*B* for $E_{\mathrm{CF}} = 4.9\,\mathrm{meV}$ and $E_{\mathrm{VBS}} = 7.9\,\mathrm{meV}$. At 200 K we observe a large reduction of the intensity of the crystal-field level at E_{CF} by $\sim 80\,\%$, whereas the intensity of the excitation at E_{VBS} already vanishes above 100 K. In contrast, a reduction of only 50% would be expected of the intensity at E_{CF} for 200 K, when thermally populating the three crystal-field excitations determined in the standard analysis, which ignores the weak mode at E_{VBS}. This situation improves slightly with a reduction of 60% at 200 K for four crystal-field levels when additionally taking into account the mode at E_{VBS}. However, the agreement is still far from satisfactory.

When additionally considering the coupling to the conduction electrons following the suggestion of ref. 59, a BFK model of crystal-field line broadening (11) provides excellent agreement with our data. The fitting procedure incorporates the code of Keller (66); for technical details see *SI Appendix*. As shown in Fig. 3*C* the improved account of the peak intensity in the BFK model is also reflected in an improved account of the energy dependence. The associated dimensionless coupling constant $g_{\mathrm{BFK}} = 0.022(0)$ is proportional to the local exchange constant and density of conduction electron states and remarkably small. While the BFK model already provides a satisfactory agreement with the broadening, further improvements may be expected when taking into account the interactions with the spectrum of phonons. A full analysis of these contributions is beyond the present capabilities of established computational techniques. As summarized in Table 1, the coupling constants g_{VBS} and g_{BFK} in $\mathrm{CeCuAl_3}$ are smaller than in $\mathrm{CeAl_2}$. This highlights that the spectrum of low-lying CEF excitations may be modified profoundly, even for systems with rather weak ME coupling.

Conclusions

In summary, we find two pronounced ME-hybrid excitations in $\mathrm{CeAuAl_3}$ beyond the Born–Oppenheimer approximation, namely a vibronic bound state and a well-resolved anticrossing. While the former was unexpected in view of previous work which did not detect a VBS in $\mathrm{CeAuAl_3}$, the latter represents a property not seen before in any intermetallic compound at zero field. Perhaps most important is the observation that both ME-hybrid excitations are due to acoustic phonons and may be resolved well, even though there is considerable damping of the CEF levels due to particle–hole excitations and the coupling constants are weak. As these observations have been made possible by means of high-resolution single-crystal neutron spectroscopy, which is generally not used in the study of CEF excitations, we conclude that ME-hybrid excitations are much more generic than hitherto assumed and must be abundant in a wide range of materials. The simplicity of our observations provides a tractable point of reference in the development of a predictive understanding of ME instabilities and functionalities in complex materials.

Materials and Methods

High-quality single-crystal $\mathrm{CeAuAl_3}$ was grown by optical float zoning under ultrahigh vacuum-compatible conditions (67). High sample purity was confirmed by means of resistivity, magnetization, and specific heat of small pieces cut from the same ingot (52, 68). The correct $\mathrm{BaNiSn_3}$-type structure and high crystalline quality were confirmed by powder and Laue X-ray diffraction as well as neutron diffraction (52). Neutron diffraction established that antisite disorder is negligible in the present samples (52), consistent with a recent NMR study (69).

Inelastic neutron-scattering measurements were carried out on the triple-axis spectrometers PUMA and PANDA at Maier-Leibnitz Zentrum (MLZ), Garching, Germany (70, 71). For the inelastic measurements a single crystal with a mass of 2 g was used. The sample was cooled with a pulse-tube cooler. All data were recorded at a temperature of 5 K unless stated otherwise, i.e., well above $T_N = 1.3$ K. For details of the experimental setup and the momentum and energy ranges covered in our experiments, refer to *SI Appendix*. The data reported in this paper are available from figshare (72).

Ab initio calculations were carried out using VASP and the frozen-core PAW method (ref. 60 and *SI Appendix*). Taking into account weak interactions of the RE ions with phonons, an expression for the hybridization of quadrupolar interactions and phonons was derived.

ACKNOWLEDGMENTS. We acknowledge discussions with P. Thalmeier, W. Wulfhekel, J. Kulda, M. Loewenhaupt, K. Becker, M. Janoschek, M. Wilde, P. Böni, and M. Klicpera. B.L. is supported by the National Natural Science Foundation of China (Grant 11875238) and Director Foundation of China Academy of Engineering Physics (Grant YZ2015009). The work of P.Č. was supported by the Czech Science Foundation (Grant 17-04925J). C.P. and A.S. acknowledge support through DFG TRR80 and DFG Grant WI3320-3. C.P. acknowledges support through European Research Council Advanced Grant 788031 ExQuiSid.

1. Eerenstein W, Mathur ND, Scott JF (2006) Multiferroic and magnetoelectric materials. *Nature* 442:759–765.
2. Snyder GJ, Toberer ES (2008) Complex thermoelectric materials. *Nat Mater* 7:105–114.
3. Santini P, et al. (2009) Multipolar interactions in f-electron systems: The paradigm of actinide dioxides. *Rev Mod Phys* 81:807–863.
4. Pfleiderer C (2009) Superconducting phases of f-electron compounds. *Rev Mod Phys* 81:1551–1624.
5. Born M, Oppenheimer R (1927) Zur quantentheorie der molekeln [On the quantum theory of molecules]. *Ann Phys* 389:457–484. German.
6. Sinha SK (1978) Magnetic structures and inelastic neutron scattering: Metals, alloys and compounds. *Metals*, Handbook on the Physics and Chemistry of Rare Earths, eds Gschneidner KA, Eyring L (North-Holland Publishing Company, Amsterdam), Vol 1, pp 489–589.
7. Vlasov KB, Ishmukhametov BKh (1964) Equations of motion and state for magnetoelastic media. *ZhETF* 19:201–212.
8. Fennell T, et al. (2014) Magnetoelastic excitations in the pyrochlore spin liquid $\mathrm{Tb_2Ti_2O_7}$. *Phys Rev Lett* 112:017203.
9. Naji M, et al. (2016) Raman scattering in $\mathrm{NpO_2}$. *J Phys Chem C* 120:4799.
10. Boldyrev KN, et al. (2017) Bifurcations of coupled electron-phonon modes in an antiferromagnet subjected to a magnetic field. *Phys Rev Lett* 118:167203.
11. Becker KW, Fulde P, Keller J (1977) Line width of crystal-field excitations in metallic rare-earth systems. *Z Phys B* 28:9–18.
12. Steglich F, Bredl CD, Loewenhaupt M, Schotte KD (1979) Antiferromagnetic ordering between unstable 4f shells in $\mathrm{CeAl_2}$. *J Phys Coll* 40:C5-301–C5-307.
13. Chapon LC, Goremychkin EA, Osborn R, Rainford BD, Short S (2006) Magnetic and structural instabilities in $\mathrm{CePd_2Al_2}$ and $\mathrm{LaPd_2Al_2}$. *Phys B Condens Matter* 378-380:819–820.

14. Adroja DT, et al. (2012) Vibron quasibound state in the noncentrosymmetric tetragonal heavy-fermion compound $CeCuAl_3$. *Phys Rev Lett* 108:216402.
15. Ruminy M, et al. (2016) Crystal-field parameters of the rare-earth pyrochlores $R_2Ti_2O_7$ (R=Tb, Dy, and Ho). *Phys Rev B* 94:024430.
16. Loewenhaupt M, Prager M, Gratz E, Frick B (1988) Magnetic excitations in $CeCu_2$. *J Magn Magn Mater* 76-77:415–416.
17. Fournier JM, et al. (1991) High-energy-neutron spectroscopy of crystal-field excitations in NpO_2. *Phys Rev B* 43:1142–1145.
18. Mentink JH, Katsnelson MI, Lemeshko M (2019) Quantum many-body dynamics of the Einstein–de Haas effect. *Phys Rev B* 99:064428.
19. Loewenhaupt M, Rainford BD, Steglich F (1979) Dynamic Jahn-Teller effect in a rare-earth compound: $CeAl_2$. *Phys Rev Lett* 42:1709–1712.
20. Loewenhaupt M, Witte U (2003) Coupling between electronic and lattice degrees of freedom in 4f-electron systems investigated by inelastic neutron scattering. *J Phys Condens Matter* 15:S519–S536.
21. Thalmeier P, Fulde P (1982) Bound state between a crystal-field excitation and a phonon in $CeAl_2$. *Phys Rev Lett* 49:1588–1591.
22. Thalmeier P (1984) Theory of the bound state between phonons and a CEF excitation in $CeAl_2$. *J Phys C Sol St Phys* 17:4153–4177.
23. Mühle E, Goremychkin EA, Natkaniec I (1989) Inelastic neutron scattering on (Pr, La)Ni_2 and (Pr, Y)Ni_2. *J Magn Magn Mater* 81:72–78.
24. Opagiste C, et al. (2011) Unconventional behavior of the $Ce_3Pt_{23}Si_{11}$ ferromagnet. *Phys Rev B* 84:134401.
25. Klicpera M, et al. (2017) Magnetic structures and excitations in $CePd_2$ $(Al,Ga)_2$ series: Development of the "vibron" states. *Phys Rev B* 95:085107.
26. Ruf T (1996) Phonon crystal-field excitations in high-T_c superconductors. *Phys B Condens Matter* 219-220:132–135.
27. Gaudet J, et al. (2018) Magnetoelastically induced vibronic bound state in the spin-ice pyrochlore $Ho_2Ti_2O_7$. *Phys Rev B* 98:014419.
28. Marshall W, Lovesey SW (1971) *Theory of Thermal Neutron Scattering: The Use of Neutrons for the Investigation of Condensed Matter*, International Series of Monographs on Physics (Clarendon Press, Oxford).
29. Güntherodt G, Jayaraman A, Batlogg G, Croft M, Melczer E (1983) Raman scattering from coupled phonon and electronic crystal-field excitations in $CeAl_2$. *Phys Rev Lett* 51:2330–2332.
30. Güntherodt G, et al. (1985) Resonant electron-phonon coupling in $CeAl_2$. *J Magn Magn Mater* 47:315–317.
31. Thalmeier P, Lüthi B (1991) The electron-phonon interaction in intermetallic compounds. *Handbook of Rare Earth Compounds*, Handbook on the Physics and Chemistry Rare Earths, ed Gschneidner KA (Elsevier, Amsterdam), Vol 14, pp 225–341.
32. Jensen J (1976) Coupling between the magnetic excitations and the phonons in praseodymium. *J Phys C Sol St Phys* 9:111–127.
33. Houmann JG, Rainford BD, Jensen J, Mackintosh AR (1979) Magnetic excitations in praseodymium. *Phys Rev B* 20:1105–1118.
34. Purwins H-G, Buyers WJL, Holden TM, Svensson EC (1976) Ground- and excited-state spin waves in $PrAl_2$. *AIP Conf Proc* 29:259–260.
35. Thalmeier P, Fulde P (1975) Rare earth systems in a magnetic field: Coupling of elastic and magnetic properties. *Z Phys B* 22:359–366.
36. Kjems JK, Hayes W, Smith SH (1975) Wave-vector dependence of the Jahn-Teller interactions in $TmVO_4$. *Phys Rev Lett* 35:1089–1092.
37. Birgeneau RJ, Kjems JK, Shirane G, Van Uitert LG (1974) Cooperative Jahn-Teller phase transition in $PrAlO_3$. *Phys Rev B* 10:2512–2534.
38. Hutchings MT, Scherm R, Smith SH, Smith SRP (1975) Inelastic neutron scattering studies of the Jahn-Teller phase transition in $TbVO_4$. *J Phys C Sol St Phys* 8:L393–L396.
39. Aksenov VL, Goremychkin EA, Mühle E, Frauenheim Th, Bührer W (1983) Coupled quadrupole-phonon excitations: Inelastic neutron scattering on van Vleck paramagnet $PrNi_5$. *Phys B+C* 120:310–313.
40. Reiffers M, Flachbart K, Beznosov AB (1988) Influence of crystal-field on the thermal conductivity of $PrNi_5$. *Czech J Phys B* 38:197–200.
41. Lawrence JM, Shapiro SM (1980) Magnetic ordering in the presence of fast spin fluctuations: A neutron scattering study of $CeIn_3$. *Phys Rev B* 22:4379–4388.
42. Loewenhaupt M, Carpenter JM, Loong C-K (1985) Magnetic excitations in CeB_6. *J Magn Magn Mater* 52:245–249.
43. Hense K, Gratz E, Nowotny H, Hoser A (2004) Lattice dynamics and the interaction with the crystal electric field in $NdCu_2$. *J Phys Condens Matt* 16:5751–5768.
44. Blackburn E, Hiess A, Bernhoeft N, Lander GH (2006) Inelastic neutron scattering from UPd_2Al_3 under high magnetic fields. *Phys Rev B* 74:024406.
45. Iwasa K, Saito K, Murakami Y, Sugawara H (2009) Electronic hybridization effect on 4*f* electron crystal field states of $PrOs_4P_{12}$. *Phys Rev B* 79:235113.
46. Iwasa K, Saito K, Murakami Y, Sugawara H (2010) Temperature evolution of crystal field splitting in Pr-filled skutterudite. *J Phys Conf Ser* 200:012071.
47. Sato NK (2001) Strong coupling between local moments and superconducting 'heavy' electrons in UPd_2Al_3. *Nature* 410:340–343.
48. Thalmeier P (2002) Dual model for magnetic excitations and superconductivity in UPd_2Al_3. *Eur Phys J B* 27:29–48.
49. Bauer ED, Frederick NA, Ho P-C, Zapf VS, Maple MB (2002) Superconductivity and heavy fermion behavior in $PrOs_4Sb_{12}$. *Phys Rev B* 65:100506.
50. Paschen S, Felder E, Ott HR (1998) Transport and thermodynamic properties of $CeAuAl_3$. *Eur Phys J B* 2:169–176.
51. Klicpera M, Javorský P (2014) Study of electronic properties in compounds, where R=Ce, La. *J Magn Magn Mater* 363:88–94.
52. Franz C, et al. (2016) Single crystal growth of $CeTAl_3$ (T= Cu, Ag, Au, Pd and Pt). *J Alloy Comp* 688:978–986.
53. Aroyo MI, et al. (2014) Brillouin-zone database on the Bilbao crystallographic server. *Acta Crystallogr A* 70:126–137.
54. Adroja DT, et al. (2015) Muon spin rotation and neutron scattering study of the noncentrosymmetric tetragonal compound $CeAuAl_3$. *Phys Rev B* 91:134425.
55. Aoki Y, Chernikov MA, Ott HR, Sugawara H, Sato H (2000) Thermal conductivity of $CeAuAl_3$: Evidence of phonon scattering by Ce magnetic moment fluctuations. *Phys Rev B* 62:87–90.
56. Klicpera M, et al. (2015) Investigation of vibron states in a $CeCuAl_3$ single crystal. Institut Laue Langevin Experimental Report 4-01-1464. Available at https://userclub.ill.eu/userclub/. Accessed March, 14, 2019.
57. Klicpera M, et al. (2017) Magnetic structure and excitations in $CeCu_xAl_{4-x}$. *Inorg Chem* 56:12839–12847.
58. Hillier AD, et al. (2012) Muon spin relaxation and neutron scattering investigations of the noncentrosymmetric heavy-fermion antiferromagnet $CeRhGe_3$. *Phys Rev B* 85:134405.
59. Tsutsui S, Kaneko K, Pospisil J, Haga Y (2017) Inelastic X-ray scattering of $RTAl_3$ (R = La, Ce, T = Cu, Au). *Phys B* 536:24–27.
60. Liu B-Q, Čermák P, Franz C, Pfleiderer C, Schneidewind A (2018) Lattice dynamics and coupled quadrupole-phonon excitations in $CeAuAl_3$. *Phys Rev B* 98:174306.
61. Balcar E, Lovesey SW (1989) *Theory of Magnetic Neutron and Photon Scattering*, Oxford Series on Neutron Scattering in Condensed Matter (Clarendon Press, Oxford).
62. Hutchings MT (1964) Point-charge calculations of energy level of magnetic ions in CEFs. *Solid State Physics*, eds Seitz F, Turnbull D (Academic, Cambridge, MA), Vol 16, p 227.
63. Bauer E, Rotter M (2009) Magnetism of complex metallic alloys: Crystalline electric field effects. *Properties and Applications of Complex Intermetallics*, Book Series on Complex Metallic Alloys, ed Belin-Ferré E (World Scientific, Singapore), Vol 2, pp 183–248.
64. Callen E, Callen HB (1965) Magnetostriction, forced magnetostriction, and anomalous thermal expansion in ferromagnets. *Phys Rev* 139:A455–A471.
65. Fulde P, Loewenhaupt M (1985) Magnetic excitations in crystal-field split 4f systems. *Adv Phys* 34:589–661.
66. Rotter M (2004) Using McPhase to calculate magnetic phase diagrams of rare earth compounds. *J Magn Magn Mater* 272-276:E481–E482.
67. Bauer A, Benka G, Regnat A, Franz C, Pfleiderer C (2016) Ultra-high vacuum compatible preparation chain for intermetallic compounds. *Rev Sci Instr* 87:013902.
68. Franz C (2014) Untersuchung von Quantenphasenübergängen bei fehlender Inversionssymmetrie [Investigation of quantum phase transitions with missing inversion symmetry]. PhD thesis (Technical Univ Munich, Munich). German.
69. Chlan V, Dolezal P, Sgallova R, Franz C, Javorsky P (2018) Local atomic arrangement in $LaCuAl_3$ and $LaAuAl_3$ by NMR and density functional theory. arXiv:1811.02871, Preprint, posted November 7, 2018.
70. Sobolev O, Park JT (2015) PUMA: Thermal three axes spectrometer. *J Large-Scale Res Facil* 1:13.
71. Schneidewind A, Čermák P (2015) PANDA: Cold three axes spectrometer. *J Large-Scale Res Facil* 1:12.
72. Čermák P, et al. (2019) Data from "Magnetoelastic hybrid excitations in CeAuAl3." figshare. Available at https://figshare.com/articles/Magnetoelastic_hybrid_excitations_in_CeAuAl3/7803092/2. Deposited March 5, 2019.